Electronic Supplementary Material (ESI) for Journal of Materials Chemistry C.

Supplementary Information

Figure S1: heatsink Confiner design

The design of the heatsink confiner is found below in figure S1A. The 2D drawing shows the spacing's between the fins that were found to be effective at cooling the side walls of the confiner to prevent the loss of the solvent vapour through the injection point. The material chosen for the confiner was stainless steel 316, and was made from a solid round bar. Figure S1B shows the actual confiner viewed from the top and then the bottom respectively along a metric ruler.

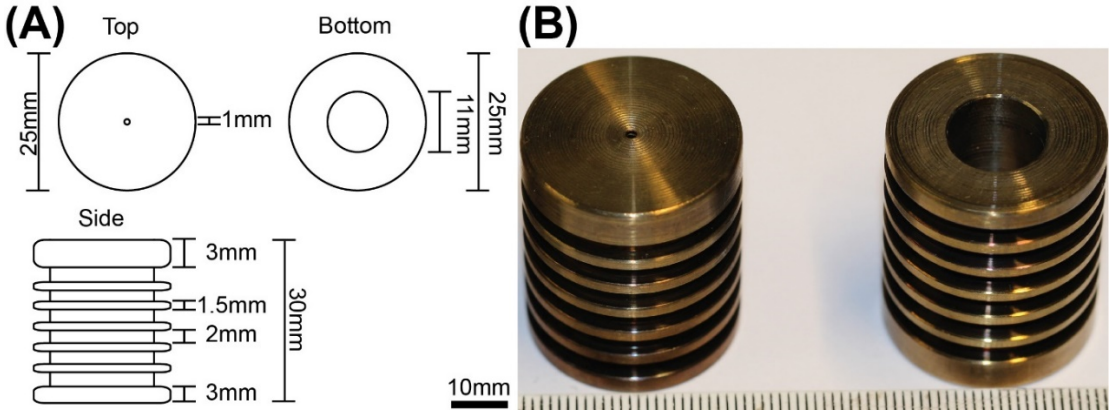

Figure S1: Confiner design with dimensions and visual example. (A) Shows the 2D drawings for the confiner along with the dimensions and spacing's used for the heatsink fins. (B) An actual image of two heatsink confiners along a metric ruler viewed from the top and then the bottom respectively.

Figure S2: Copper seeded germanium nanowires

Below is the supplementary data for copper germanide seeded germanium nanowires. Figure S2A shows the EDX element identification that was gathered for figure S2B a dark field STEM of typical large nanowire. Figure S2C shows the XRD data for the copper germanide seeded germanium nanowires dropped on a glass slide, which correspond to the phase diamond cubic germanium.

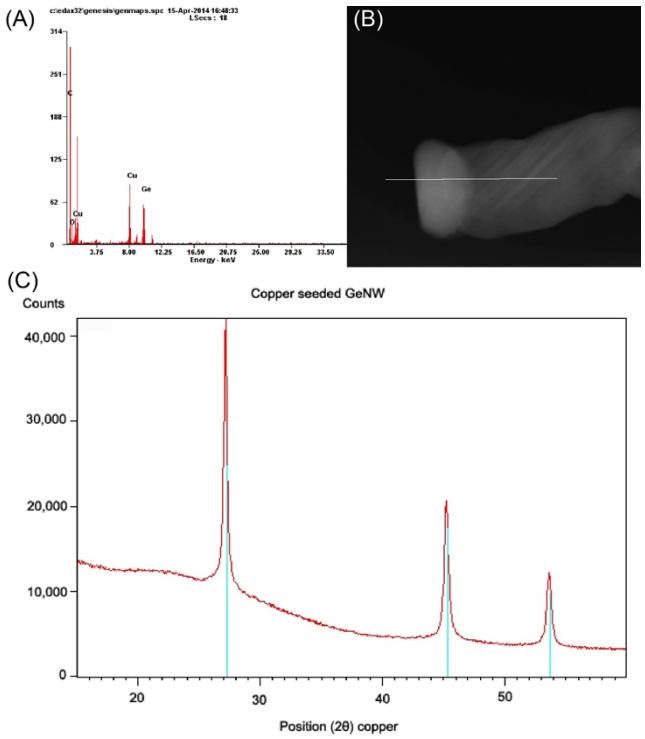

Figure S2: Copper germanide seeded germanium nanowires. (A) EDX elemental detection of nanowire seen in panel B. (B) Dark field STEM of Nanowire with copper germanide seed visible due to Z contrast. (C) XRD of c Copper germanide seeded germanium nanowires drop cast onto glass slide.

Figure S3: Production of Germanium nanowires grown in an inert environment vs germanium nanowires grown in air.

The production of germanium nanowires in air is not to be taken lightly as the reaction is extremely flammable and toxic. The same reaction condition were setup in a fume hood with appropriate safety gear and performed with minimal volume of reagent. Growth was found to occur within the reactor however, the substrate required repetitive washes with toluene to remove the hardened organic crust not found in the inert setups. HRTEM analysis of the nanowires grown in an inert atmosphere figure S3A and in air figure S3B are shown below with minimal difference between them. Small amounts of excess amorphous are present on the air reaction wires (Figure S3B) shown by the arrow. However, this could be a function of unremoved organic.

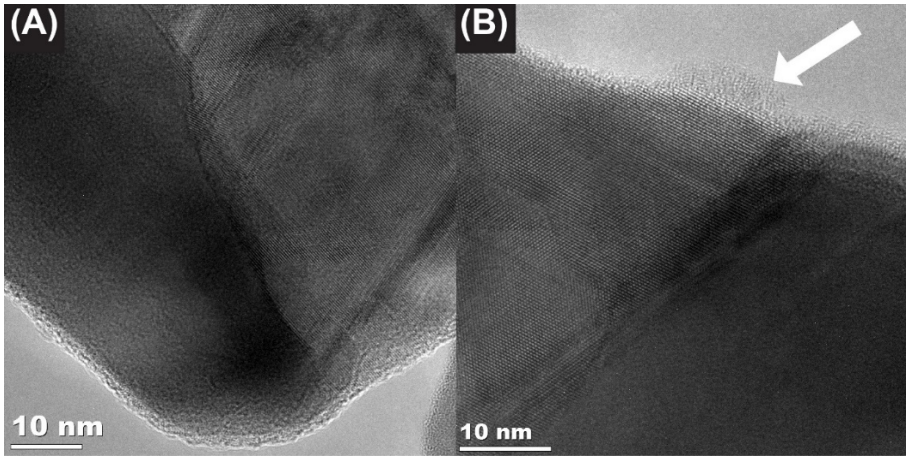

Figure S3: HRTEM of copper seeded germanium nanowires produced in (A) Inert atmosphere (B) Air atmosphere with arrow indicating very small amount of amorphous material on surface.

Figure S4: Copper silicide seeded silicon nanowires

The EDX element identification (Figure S4A) of the silicon nanowires seen in panel B shows copper and silicon percent. A HAADF STEM image of a silicon nanowires figure S4B. Silicon nanowires were sonicated from their substrate and drop cast on a glass slide before XRD figure S4C.

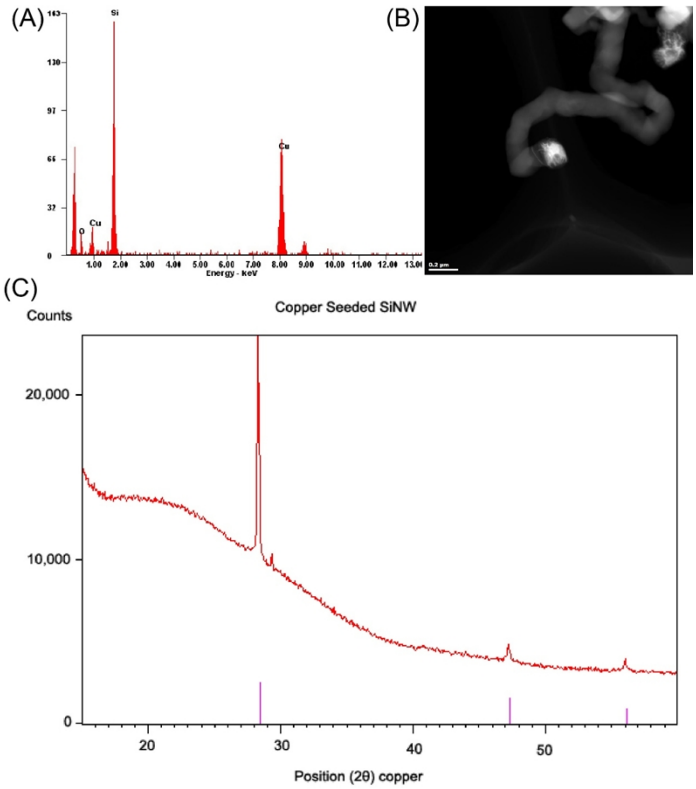

Figure S 4: Silicon nanowires grown on silicon substrate. (A) EDX elemental detection of the NW seen in panel B. (B) Dark field STEM of a typical SiNW. (C) XRD of SiNWs drop cast onto glass slide.

Figure S5: Agglomeration of copper during annealing on a silicon wafer.

The copper thin film was thermally evaporated as stated in the methods. Figure S5 below shows the copper film after evaporation before any anneal process.

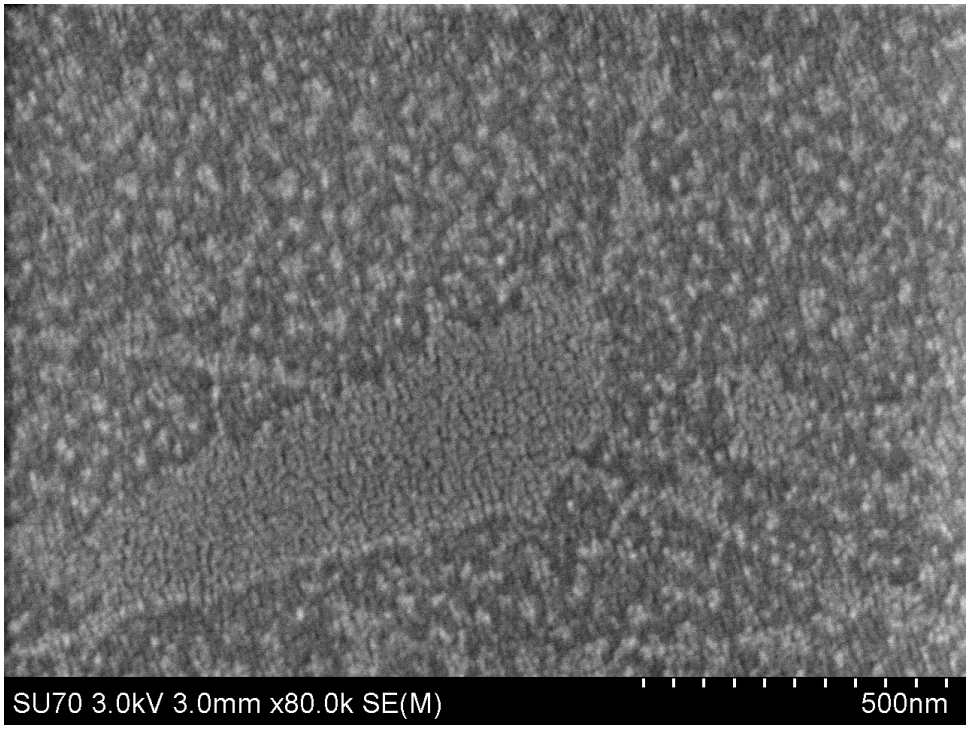

Figure S5: Copper film after thermal evaporation onto a silicon wafer.

Figure S6: Copper seeded $Si_{1-x}Ge_x$ nanowires

The element identification of $Si_{1-x}Ge_x$NWs using EDX is seen in figure S6A of the corresponding dark field STEM of the NW in figure S6B. A multipoint EDX elemental quantification was performed along the $Si_{1-x}Ge_x$NWs. The data collected is tabulated below where 1-3 is the larger $Si_{1-x}Ge_x$NW and 4-5 corresponds to the $Si_{1-x}Ge_x$NW. XRD of the $Si_{1-x}Ge_x$NWs show peak splitting unique to the alloy NW is seen in Figure S6C, possibly due to the mixed population.

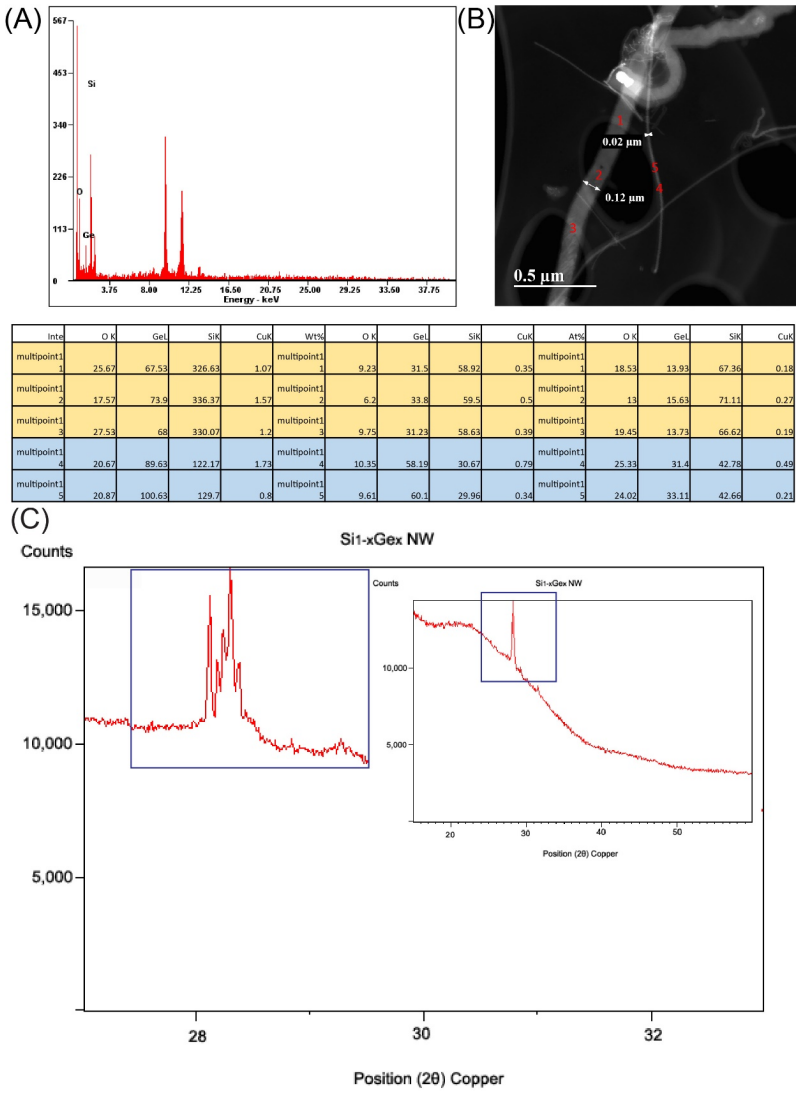

Inte	O K	GeL	SiK	CuK	Wt%	O K	GeL	SiK	CuK	At%	O K	GeL	SiK	CuK
multipoint1 1	25.67	67.53	326.63	1.07	multipoint1 1	9.23	31.5	58.92	0.35	multipoint1 1	18.53	13.93	67.36	0.18
multipoint1 2	17.57	73.9	336.37	1.57	multipoint1 2	6.2	33.8	59.5	0.5	multipoint1 2	13	15.63	71.11	0.27
multipoint1 3	27.53	68	330.07	1.2	multipoint1 3	9.75	31.23	58.63	0.39	multipoint1 3	19.45	13.73	66.62	0.19
multipoint1 4	20.67	89.63	122.17	1.73	multipoint1 4	10.35	58.19	30.67	0.79	multipoint1 4	25.33	31.4	42.78	0.49
multipoint1 5	20.87	100.63	129.7	0.8	multipoint1 5	9.61	60.1	29.96	0.34	multipoint1 5	24.02	33.11	42.66	0.21

Figure S 6: $Si_{1-x}Ge_xNW$. (A) EDX elemental identification with both silicon and germanium present form panel B. (B) Dark field STEM image of large and thin NW. Multipoint line scan analysis of NWs with large $Si_{1-x}Ge_xNW$ corresponding to points 1-3 and thin $Si_{1-x}Ge_xNW$ corresponding to point 4-5 tabulated below. (C) XRD pattern from $Si_{1-x}Ge_xNWs$, with peck splitting observed.

Figure S7: Additional data on patterned nanowire anodes

The application for dense NWs on current collectors are attractive for lithium ion battery applications. To demonstarte the materials application germanium nanowires were patterned and setup as follows. Electrode substrates of stainless steel were roughened with fine sand paper before cleaning extensively in toluene and acetone. Samples where then placed into the MB-EcoVap Mbraun integrated thermal evaporator where a coating of 1-10 nm of copper was applied to the substrates. 7x7 mm squares where cut and weighed on a Sartorius Ultra-microbalance model SE2 (Error of ±0.1µg), before reacting in a SVG confiner. Reacted substrates were then soaked overnight in toluene to remove any residual organic materials.

Gravimetric nanowire weights were then recorded using the same ultra-microbalance. The electrochemical performance was then measured by assembling Swagelok cells with the sample separated by a porous polyethene separator and lithium ion counter, with of 1M LiPF6 in ethylene/dimethyl carbonate (1:1 v/v) +3wt% vinylene carbonate. All measurements were taken on the Biologic MPG-2 within the range of .01-1.5 V versus Li/Li+The production of the patterned electrode anodes for the half cell setup is described in the methods of chapter. A SEM image of one of the patterned electrodes is seen below (Figure S7A), with strips of active nanowire material running along the stainless steel surface. High resolution SEM image of the wires within this strip are shown below (Figure S7B).

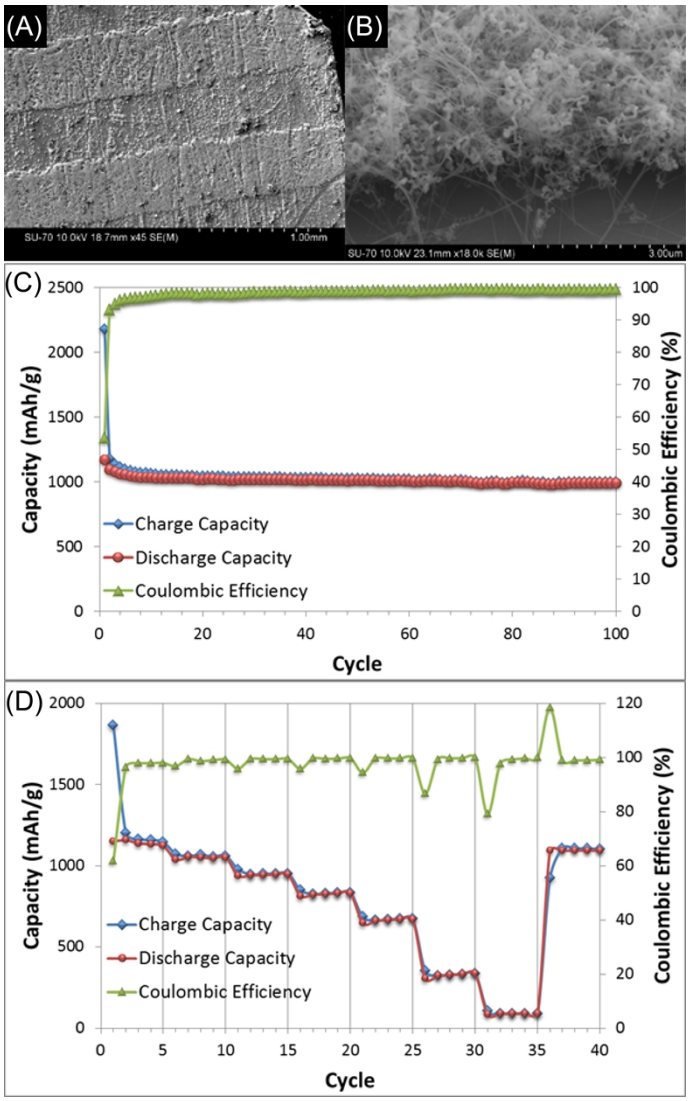

Figure S 7: SEM of Electrode (A) showing the strips of grown material on the stainless steel. (B) A tilted SEM image of the wires produced in the strips. (C) Charge capacity, discharge capacity and columbic efficiency of a Ge NW electrode cycled at a rate of C/5 in the voltage range of 1.0–0.01 V. (D) Rate capability experiments of Ge NW electrodes cycled at rates of C/10, C/5, C/2, 1C, 2C, 5C, 10C and back to C/10. The electrodes were cycled in the voltage range of 1.5– 0.01 V

The suitability of Ge as a Li-ion battery anode material has received a lot of research interest of late, owing to its high-capacity (1384 mAh/g) compared with conventional graphitic-based anodes (372 mAh/g). Furthermore, the high conductivity, short Li-ion diffusion distances and high rate of Li diffusion inherent to GeNWs make them suitable for high power rate applications. To test the performance of the patterned GeNW substrates synthesised using the heatsink confiner as a Li-ion anode material, two electrode Swagelok-type cells were set up with the patterned GeNWs on SS as the working electrode and Li metal as both the counter and reference electrode. A patterned working electrode was fabricated consisting of 5 strips of GeNWs 700 µm x 7 mm spaced 700 µm apart (Supplementary Figure S7A). The GeNW electrode was cycled at a C/5 rate in the voltage range of 1.0 – 0.010 V. The electrode performed very well exhibiting a capacity of 993 mAh/g after 100 cycles and a columbic efficiency of 99.5% (Figure S7C). The rate capability was also evaluated by charging and discharging the material for 5 cycles at rates of C/10, C/5, C/2, 1C, 2C, 5C, 10C and then back to C/10 (Figure S7D). The electrode exhibited capacities of 1122, 1050, 946, 829, 669, 334, 89, and 1092 mAh/g at each respective rate, notably recovering 97% of its original capacity when reverting back to the slower rate of C/10.